JAMES | Journal of Advances in Modeling Earth Systems

RESEARCH ARTICLE
10.1029/2023MS003712

Implementation of the Novel Duo-Grid in GFDL's FV3 Dynamical Core

Joseph Mouallem[1,2], Lucas Harris[2], and Xi Chen[3]

[1]Cooperative Institute for Modeling the Earth System, Program in Oceanic and Atmospheric Sciences, Princeton University, Princeton, NJ, USA, [2]NOAA/Geophysical Fluid Dynamics Laboratory, Princeton, NJ, USA, [3]Institute of Atmospheric Physics, Chinese Academy of Sciences, Beijing, China

Key Points:

- A new cubed-sphere grid structure, the "Duo-Grid," is implemented in the Geophysical Fluid Dynamics Laboratory's Dynamical Core (FV3)
- The Duo-Grid remaps data along cube edges and synchronizes fluxes to rectify the "kink" in the coordinates
- Grid imprinting of the cubed sphere is greatly reduced in idealized tests and FV3's accuracy and robustness have improved

Correspondence to:
J. Mouallem,
mouallem@princeton.edu

Citation:
Mouallem, J., Harris, L., & Chen, X. (2023). Implementation of the novel Duo-Grid in GFDL's FV3 dynamical core. *Journal of Advances in Modeling Earth Systems*, *15*, e2023MS003712. https://doi.org/10.1029/2023MS003712

Received 7 APR 2023
Accepted 9 NOV 2023

Author Contributions:
Conceptualization: Joseph Mouallem, Lucas Harris, Xi Chen
Data curation: Joseph Mouallem
Formal analysis: Joseph Mouallem
Funding acquisition: Lucas Harris
Investigation: Joseph Mouallem
Methodology: Joseph Mouallem, Lucas Harris, Xi Chen
Project Administration: Joseph Mouallem
Resources: Lucas Harris
Software: Joseph Mouallem, Xi Chen
Validation: Joseph Mouallem
Visualization: Joseph Mouallem
Writing – original draft: Joseph Mouallem, Lucas Harris

Abstract The gnomonic cubed-sphere grid has excellent accuracy and uniformity, but the "kink" in the coordinates at the cube edges in the halo region can leave an imprint of the cube in the solution, and requires special edge handling. To reduce grid imprinting, we implement the novel "Duo-Grid" within the Geophysical Fluid Dynamics Laboratory's (GFDL) Finite-Volume Cubed-Sphere Dynamical Core (FV3). The Duo-Grid remaps a cube face's data from neighboring face from kinked to natural locations along great circle lines using 1D piecewise linear interpolation. A 2D interpolation algorithm is used to fill correct data at the eight corners of the cubed-sphere needed for FV3's 2D advection scheme. The Duo-Grid was tested in idealized tests using the 2D shallow water solver and the 3D hydrostatic and non-hydrostatic solvers. We found that error norms are greatly reduced and grid imprinting is practically eliminated when employing the Duo-Grid. These results indicate that FV3's accuracy and robustness have improved.

Plain Language Summary In Computational Fluid Dynamics (CFD), numerical solutions should ideally be grid-independent, so that grid choice should have no noticeable effects on flow behavior. However, designing complex CFD codes in general and atmospheric dynamical cores in particular necessitates a series of design decisions that balance the code numerical efficiency and accuracy. In GFDL's dynamical core FV3, unphysical structures from the gnomonic cubed-sphere grid structure, such as edges and corners, can appear in the numerical solution especially at lower resolutions and in long climate simulations. This is known as grid imprinting which is due to errors in the assumed location of grid cells on opposing sides of a cube edge. While this assumption is computationally inexpensive, it creates a grid imprinting problem especially for low resolution simulations. In this paper, we implement a new algorithm called Duo-Grid that corrects the location of the cross-edge data, and eliminates grid imprinting in FV3. The increase in accuracy comes at the expense of additional computational complexity.

1. Introduction

Dynamical core development entails trade-offs between computational accuracy and performance. In the case of the Geophysical Fluid Dynamics Laboratory (GFDL)'s Finite-Volume Cubed-Sphere Dynamical Core (FV3), global simulations use the gnomonic cubed-sphere grid, which was found by Putman and Lin (2007) to be one of the most uniform regular quadrilateral grid with a spherical topology, allowing for the highly competitive timestep and most accurate solution compared to cubed-spheres with the same number of cells. The trade-offs of using the gnomonic cubed-sphere is that the local coordinates are non-orthogonal, and the coordinates have "kinks" at the edges of the cube in the halo region. The non-orthogonality is addressed by a revision of the fundamental algorithms but the kinks represent a significant discontinuity that can create visible artifacts along the edges and corners in the solution. These artifacts are called "grid imprinting." A simple correction is applied by Putman and Lin (2007) to reduce the imprinting but it is still noticeable especially at the lower resolutions used for global climate modeling.

Grid imprinting is a natural numerical phenomena caused by grid discontinuities or strong curvature of grid coordinate lines (Rančić et al., 2017). Any grid type on a sphere is not perfect and presents some kind of discontinuity. A cubed-sphere grid has discontinuities at the cube's edges and corners. These discontinuities generate artifacts and noise in the numerical solution at the location of the grid discontinuities. This noise will manifest some of the grid shape in the numerical solution thus the name grid imprinting.

Writing – review & editing: Joseph Mouallem, Lucas Harris, Xi Chen

Several researchers have mentioned the FV3 grid imprinting issue in their work. Zhao et al. (2018) reported a distortion in the climatological-mean precipitation near the edges of the cubed-sphere grid in two FV3-based atmosphere climate models, AM3 and AM4. They showed that the distortion was less pronounced in AM4, presumably due to the higher resolution used compared to AM3. Other researchers reported the same issue in their cubed-sphere dynamical cores (Rančić et al., 2017). In addition, other grid types exhibit a grid imprinting issue as well. Weller et al. (2012) studied grid imprinting on five quasi-uniform spherical C-grids using the TRiSK scheme. Peixoto and Barros (2013) analyzed the sources of grid imprinting on geodesic spherical icosahedral grid and showed that grid imprinting errors are caused by the slow convergence on badly aligned cells. Whitaker (2015) found all considered grid types in several dynamical cores presented a certain level of grid imprinting, exhibited grid related numerical noise and introduced computational modes at the grid scale which grew with simulation time and contaminated the large scale modes in the numerical solution, most notably in a baroclinically unstable atmosphere in which small perturbations due to imprinting can rapidly grow.

A highly efficient method called the "Duo-Grid" was introduced by Chen (2021) to address grid imprinting in gnomonic cubed-sphere grids. The Duo-Grid implements two grids on each face of the cubed-sphere: a "kinked" grid which follows the coordinate on the facing grids and includes the discontinuous coordinate, and an "extended" grid which extends the face's coordinates onto the facing grids along great circle lines. Chen (2021) applied the Duo-Grid to their unstaggered dynamics to reduce the amplitude of grid imprinting into imperceptibility. Other researchers have investigated a similar approach as well, but these methods only apply to the equiangular gnomonic cubed-sphere grid, and not optimized for performance (Katta et al., 2015; Ullrich et al., 2010).

In this work, we implement the Duo-Grid system in FV3 to mitigate this grid imprinting issue. In Section 2, we present a brief overview of FV3's design and numerics prior to describing the Duo-Grid algorithm. Subsequently, Section 3 presents results for different idealized tests using both the shallow water and the 3D non-hydrostatic solvers, featuring different flow configurations, advection schemes and grid resolutions. Section 4 provides an overview of the ongoing work, while Section 5 concludes the paper.

2. Model Description

2.1. FV3 Dynamical Core

FV3 is a nonhydrostatic Finite-Volume Cubed-Sphere Dynamical Core that has been under development at GFDL for more than two decades (Chen et al., 2013; L. M. Harris et al., 2016; L. M. Harris & Lin, 2013; Lin, 2004; Lin & Rood, 1996, 1997; Mouallem et al., 2022; Putman & Lin, 2007). It is used in many weather and climate models for a wide range of applications from short-term weather forecasts to centuries-long climate simulations, moving-nest hurricane forecasts, chemical and aerosol transport modeling, cloud-resolving modeling, and so on. FV3 solves the non-hydrostatic compressible Euler equations on gnomonic cubed-sphere grid with a Lagrangian vertical coordinate. The algorithm is fully explicit except for fast vertically propagating sound and gravity waves which are solved by the semi-implicit method. The long time-step of the entire solver is called *dt_atmos* which also corresponds to the physics time-step. The number of vertical remapping loops for each *dt_atmos* is defined by *k_split* where subcycled tracer advection is also performed. The acoustic time-step is defined by *n_split* per remapping loop yielding an acoustic time-step of $dt\_atmos/(k\_split \times n\_split)$ where sound and gravity wave processes are advanced and thermodynamics variables are advected. The detailed description of the solver's horizontal and vertically Lagrangian discretizations can be found in Lin and Rood (1996), Lin and Rood (1997), and Lin (2004).

2.2. FV3's Numerics Overview

FV3's numerics are extensively described in Section 2 and 3 in Lin and Rood (1996) and later on in Lin and Rood (1997), Lin (2004), and Putman and Lin (2007). A quick summary is provided here, based on the aforementioned references, to allow readers understand the need of different halo remapping procedures for different grid staggering and corners as described in the next section.

FV3 uses a multidimensional flux-form advection scheme of Putman and Lin (2007), which is a multidimensional extension of traditional 1-D finite-volume schemes. Multidimensionality is achieved through a successive application and cross-averaging of 1D operators, eliminating the leading order deformational error and improving the

stability of the scheme. This method requires data across the kinked edges and in the corners of the cubed-sphere, which is typically done by simply copying data from the adjacent cube face, and by performing an average of two symmetric extrapolations to the cube edges to reduce grid imprinting (Putman & Lin, 2007).

FV3's horizontal discretization uses the C-D grid system, allowing for exact diagnosis of cell-mean vorticity and accurate calculation of fluxes. In this system, in addition to the prognostic cell-mean scalars (A-grid) and D-grid staggered winds, diagnosed face-perpendicular (C-grid) winds, cell-mean (A-grid) vorticity, and grid-corner (B-grid) kinetic energy and divergence are all needed to advance the prognostic equations; see details in Lin and Rood (1997). As a result, the FV3 algorithms require variables defined on all four grids and the edge handling and/or Duo-Grid need to handle all of these staggerings:

- A-grid cell centered quantities such as height and vorticity
- B-grid corner quantities such as divergence and kinetic energy
- C-grid cell face perpendicular velocities used for fluxes and diagnosed advective winds
- D-grid cell face tangential velocities used for prognostic winds.

Additional information on different grid staggering layouts and techniques can be found in Arakawa and Lamb (1977) and in particular, their Figure 3 shows the spatial distributions of the dependent variables on a square grid.

2.3. Duo-Grid

In this work, we implement an extension of the Duo-Grid developed by Chen (2021) in their Low Mach number Approximate Riemann Solver (LMARS). LMARS with the Duo-Grid is a highly efficient unstaggered finite-volume solver for the horizontal advection equations on arbitrary gnomonic cubed-sphere grids. The Duo-Grid algorithm in LMARS supports halo remapping of cell centered scalars and unstaggered vectors. LMARS does not need a corner handling algorithm since it does not employ a 2D transport scheme similar to the 2D FFSL of Lin and Rood (1996). As a result the implementation of the Duo-Grid in LMARS is relatively simple.

FV3, on the other hand, requires all of the above: a halo extension and remapping for cell centered variables, C/D staggered winds, and cell corner variables. Moreover, an algorithm for the corner ghost regions for different grid staggering is also needed due to the 2D FFSL transport scheme as explained in the previous section. For the edges, we extend the original Duo-Grid code to support different grid staggerings, including cell corner variables (B grid) and C/D winds. For the cubed-sphere corners, we implement the two-dimensional interpolation of Zerroukat and Allen (2022) to fill the corner ghost regions with correct data. The halo extension and remapping of staggered vectors are not trivial. Consider the D grid winds: For a C[N] grid (N denotes the number of cells in one horizontal direction, so each face of the cubed-sphere has NxN grid cells), the local velocities U and V in the local x- and y-directions, respectively, are offset. The velocity components are non-coincident and tangential to the grid cell faces: U tangential to the (local) north and south faces while V tangential to the east and west faces and as a result there is an extra U velocity in the y-direction and an extra V velocity in the x-direction. The Duo-Grid extension for such field consists of the following steps:

1. Project the local velocities U and V to the center or (A-grid) location in local coordinates.
2. Rotate the local velocities into the earth-relative zonal and meridional winds. (This is an exact transformation.)
3. Remap the earth-relative winds from kinked to extended grid locations.
4. Rotate the earth-relative winds back to the local velocities, again done exactly.
5. Project the local velocities back to the appropriate grid cell faces to obtain the remapped U and V fields in local cubed-sphere coordinates.

To conserve symmetry, this process require four halo points in local coordinates to get a final three halo remapped velocity fields. Same logic applies for C-grid winds.

The existing edge handling in FV3 (Putman & Lin, 2007) performs a simple extrapolation directly on the data at the edges and corners of a face simply copied from native data on the opposing faces. This process consists of simple MPI communications or data copying among the corresponding processors with no additional computational overhead. While this presents a huge advantage in computational performance for massive parallel runs, it introduces numerical errors in the solution due to the usage of "kinked-grid" data instead of data that should lie along the extended great circle lines of a face as shown in Figure 1 by the yellow dashed lines. To be exact, the term "kinked grid" refers specifically to the area within the halo region where the grid displays a kinked pattern

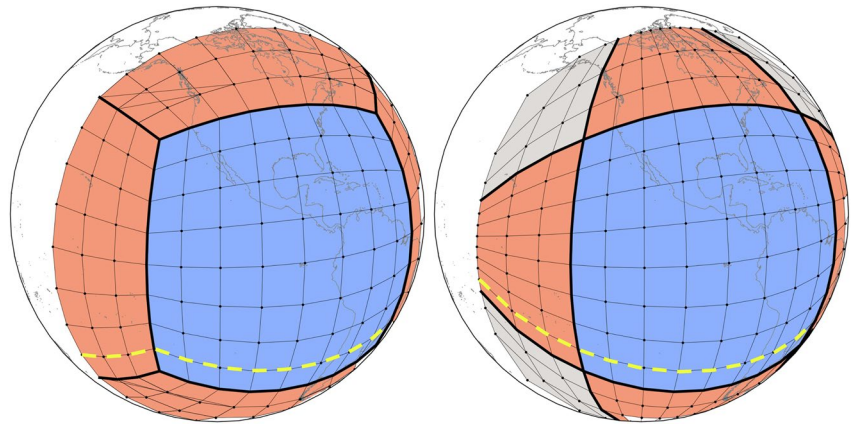

Figure 1. C8 cubed-sphere grid with a three-cell halo. Left: "kinked" grid showing halo updated directly from the neighboring face. Right: "extended" grid for the forward face showing data remapped onto the extended grid. Note that the great circle coordinate lines extend from the compute domain into the grid halo without interruption.

(and could also be called "kinked haloes"), rather than the entire grid. However, for the sake of simplicity, we will use the term "kinked grid" in this paper. The Duo-Grid remaps data from its "kinked-grid" location on a neighboring face to its corresponding natural location on extended great circle lines, called the "extended grid." This is discussed in detail in Chen (2021). In addition, they used a 1D piecewise linear interpolation in their remapping algorithm and found no degradation compared to high-order 1D polynomial remapping algorithms, thus, we will use the same interpolation method. Consequently, no edge handling code is required when using the Duo-Grid, given the absence of the "kinked grid" discontinuity—all calculations can be done on the extended grid. While this improves the quality of the numerical solution since all noise due to the edges and corners is eliminated, it introduces substantial computational overhead due to (a) the halo remapping process at every halo update of a variable of interest (b) the edge flux synchronization between different faces to ensure conservation of different quantities such as mass.

It is critical to recognize that edge flux synchronization and halo remapping are two distinct processes: Consider two adjacent faces A and B. The operation of computing fluxes on a kinked grid at the edge of face A is identical to that of face B. That is, the halo region of face A, at the common A/B edge, is populated from face B by simply copying data from face B. Similarly, the halo region of face B is populated by copying native data from face A. Since, the 2D FFSL scheme is free of directional bias, the resulting fluxes computed on either face A or face B are identical since the input data is identical. Therefore, no flux adjustment is required. On the other hand, in the case of the Duo-Grid, the halo data of face A is remapped from data of face B, and vice versa for face B, resulting in different input data for the 2D FFSL operators and thus different flux values on each side of the edge. This is illustrated in Figure 2. Therefore, to ensure conservation of mass and scalars, the resulting fluxes are exchanged between faces A and B and then averaged. This includes additional MPI communications among the processors lying along the edges.

To ensure flux synchronization in FV3, the subroutine d_sw(), which computes the forward time-step of the prognostic winds on the D-grid and updates the dynamical scalars, is broken into several smaller subroutines where the computation and application of fluxes of different components are separated. Flux synchronization among different faces is then applied right after the computation of the aforementioned fluxes at every acoustic time-step for different quantities such as those used to update mass, tracers, and the components related to kinetic energy and vorticity from which the prognostic D-grid winds are built. For more technical information about the FV3 time-integration, please refer to (L. Harris et al., 2021).

It is worth noting that not all models are inherently mass conserving and some require applying mass fixers to ensure mass conservation (Diamantakis & Agusti-Panareda, 2017). For short term weather forecast applications, flux synchronization could be simply turned off since mass conservation is not an ultimate priority.

3. Simulations and Results

We first test the FV3 Duo-Grid implementation with the shallow-water solver. Most of the 2D shallow water idealized runs are based on Williamson (1992)'s test cases, which are commonly used in traditional dynamical

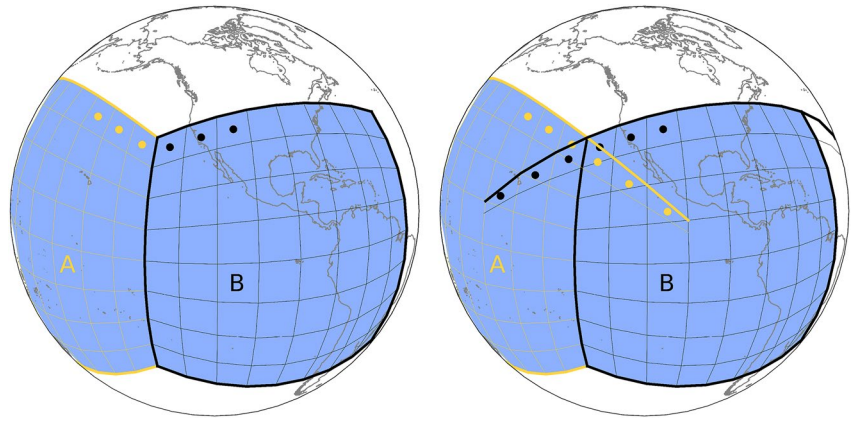

Figure 2. C8 cubed-sphere grid with a three-cell halo. Left: "kinked" grid showing halo updated directly from the neighboring face, yielding same flux values on each side of the edge of opposing faces. Right: "extended" grid showing data remapped onto the extended grid, resulting in different flux values on each side of the edge of opposing faces. Only one data line is shown.

core testing. Different flow configurations, grid resolutions, and advection schemes are tested. We later test the 3D hydrostatic and non-hydrostatic solvers to show the effects of the Duo-Grid in more realistic simulations. Output from all simulations and resolutions are regridded to 360 × 180 longitude-latitude resolution for making plots and computing error norms.

The primary goal of these tests is to demonstrate that the Duo-Grid algorithm reduces noise and grid imprinting in the numerical solution without degrading the solution in the interior of the faces. In some cases, we will in fact find that the interior solution is improved with the Duo-Grid. To quantify these errors, we use error norm measures as defined in Williamson (1992), Chen (2021). We also plot error maps to show the spatial distribution of these errors relative to the flow and grid configurations in different cases. The area weighted error norms (or loss functions) are:

$$l_1(h) = \frac{I(|h - h_T|)}{I(|h_T|)} \tag{1}$$

$$l_2(h) = \sqrt{\frac{I\left((h - h_T)^2\right)}{I\left(h_T^2\right)}} \tag{2}$$

$$l_\infty(h) = \frac{\max|h - h_T|}{\max|h_T|} \tag{3}$$

where

$$I(h) = \frac{\Sigma h \Delta A}{\Sigma \Delta A} \tag{4}$$

and h is the fluid height, h_T the true solution of the fluid depth, ΔA the local grid cell are, and the sum is over all grid cells on the domain. If no analytical solution is available, h_T will be taken from the highest resolution simulation.

3.1. Shallow Water Solver

Four tests for the 2D shallow water solver are presented here: the steady state geostrophic balanced flow (case2), the splash on the sphere, the Rossby-Haurwitz wave (case6) and the colliding modons (case8). We test layouts in which the flow is first perpendicular to the edges ($\alpha = 0$) then oriented over a cubed-sphere grid corner ($\alpha = 45$). The list of advection schemes is shown in Table 1 along with their damping coefficients if present. For a C48 grid, which corresponds to a resolution of 200 km, we use an acoustic time-step of 512 s unless stated otherwise for a specific case. We use sixth-order divergence damping with a non-dimensional coefficient of 0.12.

Table 1
Advection Schemes and Vorticity Damping Options Used in This Manuscript

Name	Label	Type	Vorticity damping	Vorticity damping coef
Unlimited "fifth-order" scheme with $2\Delta x$ filter	UNLIM	Linear	T	0.06
Intermediate-strength $2\Delta x$ filter	MINDIFF	Linear	T	0.06
PPM with Lin, 2004's constraint	MONO	Monotonic	F	0
PPM with Hunyh's constraint and $2\Delta x$ filter	HUYNH	Monotonic	F	0

Figure 3 illustrates the time evolution of error norms for a 5-day 2D steady-state geostrophic balanced flow oriented perpendicular to the edges ($\alpha = 0$). Here, the exact solution used to compute error norms is the initial flow state, and any deviation from the initial field is considered an error. As can be seen, the Duo-Grid produces smaller errors throughout the whole simulation time for all advection schemes and all errors norms. The same is true for the flow over the corners (Figure 4) and indeed the Duo-Grid's errors are very similar for both flow orientations, while the $\alpha = 45$ flow shows significantly larger errors on the kinked grid. This means that the Duo-Grid is practically indifferent of the flow orientation, which is not the case for the kinked grid. It is worth noticing the significant sensitivity in l_∞ when varying the flow orientation and advection schemes, particularly the case of "MINDIFF" where l_∞ is one magnitude lower when using the Duo-Grid.

Figures 5 and 6 display the spatial distribution of errors measured for the meridional velocity and surface pressure for the steady state geostrophic balanced flow using the advection scheme 'MONO' on days = 1, 3 and 5. In this case, any deviation from the fields at the initial conditions $t = 0$ is considered an error. As seen in the figures, errors in the kinked grid case are generated at the edges and corners of the cubed-sphere grid then propagate and contaminate the whole numerical field. These errors are much smaller in the Duo-Grid case which is consistent with the plots of time evolution of error norms shown above.

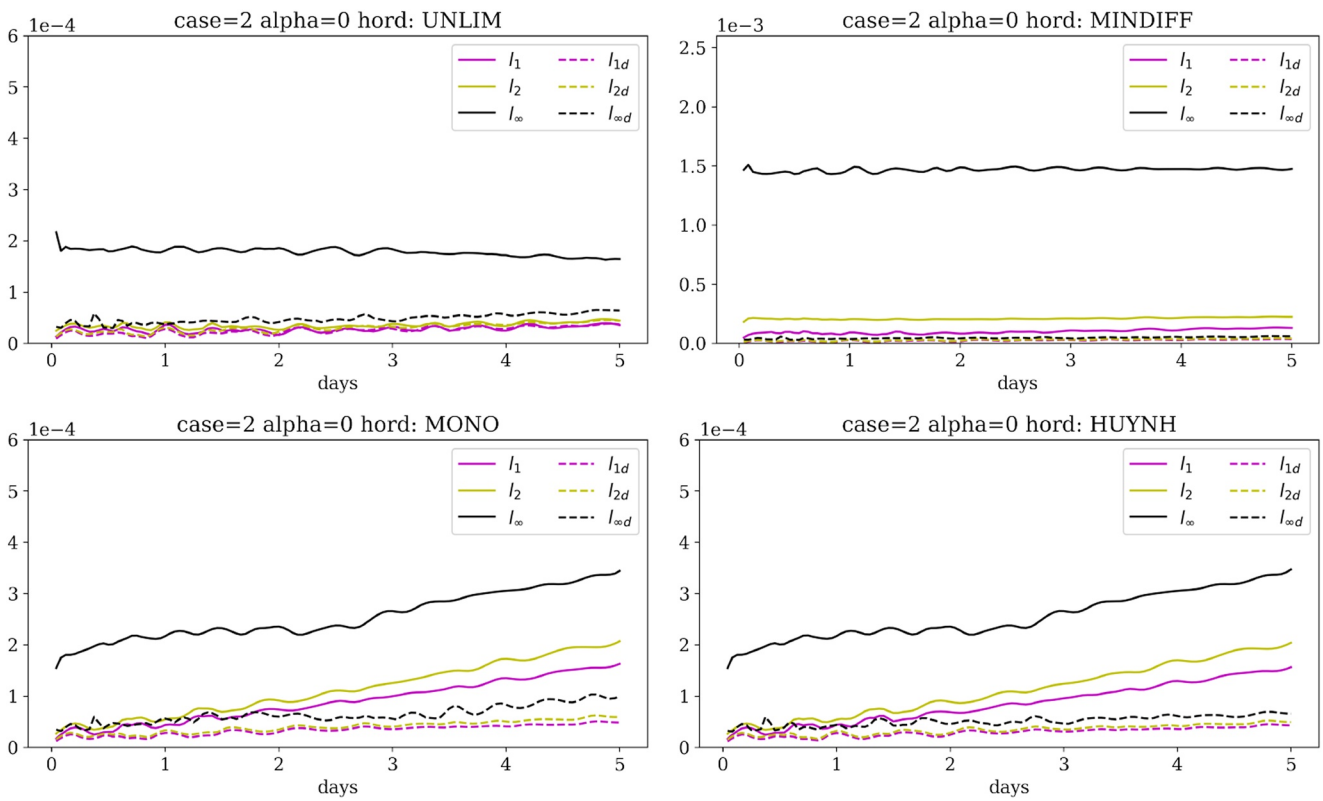

Figure 3. Time evolution of error norms l_1, l_2, l_∞ for the C48 steady state geostrophic flow and a flow oriented perpendicular to the cubed-sphere edges $\alpha = 0$. Error norms obtained on the kinked grid are represented by solid lines while those on the Duo-Grid are represented by dashed lines.

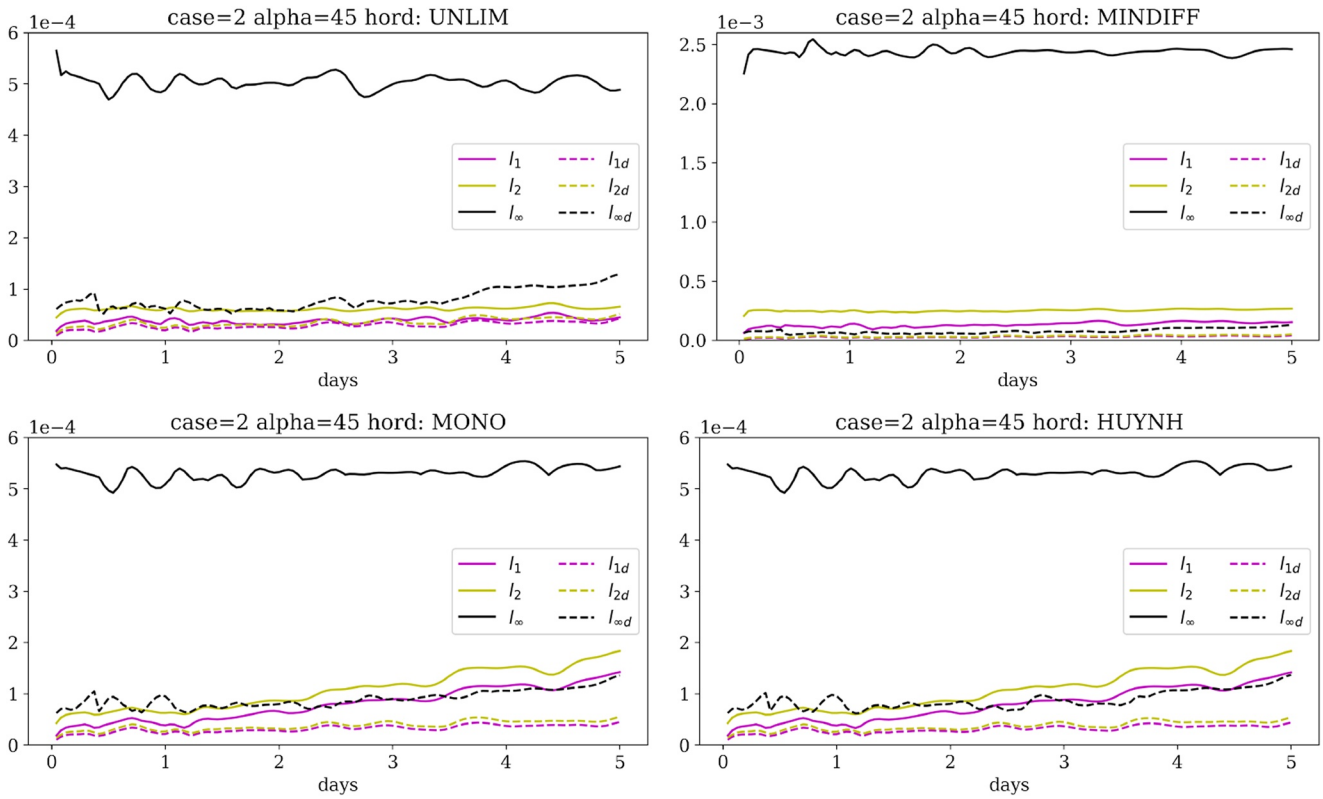

Figure 4. As in Figure 3 but for $\alpha = 45$.

Figure 7 shows the convergence of error norms l_1, l_2, l_∞ at day 5 for the steady-state geostrophic balanced flow oriented perpendicular to the edges $\alpha = 0$ for grid resolutions C48 (200 km), C96 (100 km), C192 (50 km), C384 (25 km) and C768 (13 km). The advection scheme used here is 'MONO'. Similar to the previous C48 results, the runs employing the Duo-Grid have lower errors compared to those without it for the same resolution from C48 to C768. In addition, the magnitude of all error norms systematically decreases across all resolutions from C48 to C768. It is worth noting that in the case of the Duo-Grid, a second order convergence rate is conserved for all errors norms across all resolutions, while it is severely degraded in the original solver especially the case of l_∞ where it is around 0.23. This clearly indicates that the Duo-Grid greatly improves the convergence rate of the solution: removing the edge error reveals the true order of accuracy of FV3's horizontal discretization.

The "Splash on the Sphere" test was introduced by Chen (2021) to evaluate numeric solvers' capabilities in faithfully representing wave propagation speeds and amplitudes. The splash test initializes a sinusoidal droplet at the North Pole that freely propagates on the non-rotational sphere. Therefore, a perfect model should present zero zonal wind. However, cubed-sphere models inevitably inherit metric errors from the curvilinear geometry, for example, the computational cells are not perfect parallelograms. Hence, observing the evolution of the zonal wind can serve as a unique metric for errors related to computational grid geometry. Figure 8 shows zonal winds on days 6, 7.5, and 14 from the original solver on the left and the Duo-Grid on the right. Strong grid imprinting is presented from the original solver on a full-sphere distribution, indicating possible noise production from the cubed-sphere tile edges. The Duo-Grid solver alleviates such problems, and the errors are mostly limited near the splash signals. It is also worth pointing out that some 2-delta noise from the original solutions is primarily handled smoothly from the Duo-Grid solutions. Figure 9 is identical to Figure 8, except the meridional wind is presented. At a low resolution of C48, ripples behind the splash wave due to geometry errors can still be observed. The results from the kinked-grid show more ripples behind the wavefront while the Duo-Grid results illustrate better control of the numerical noise away from the main signals. One may wonder if the Duo-Grid solver achieves this reduction of the artifacts by being more diffusive or by introducing dispersion errors. Figure 10 demonstrates the evolution of both solvers' peak flow height and meridional winds. The differences are not noticeable, indicating that the Duo-Grid does not affect the dissipation and dispersion characteristics of FV3. Therefore, the splash test

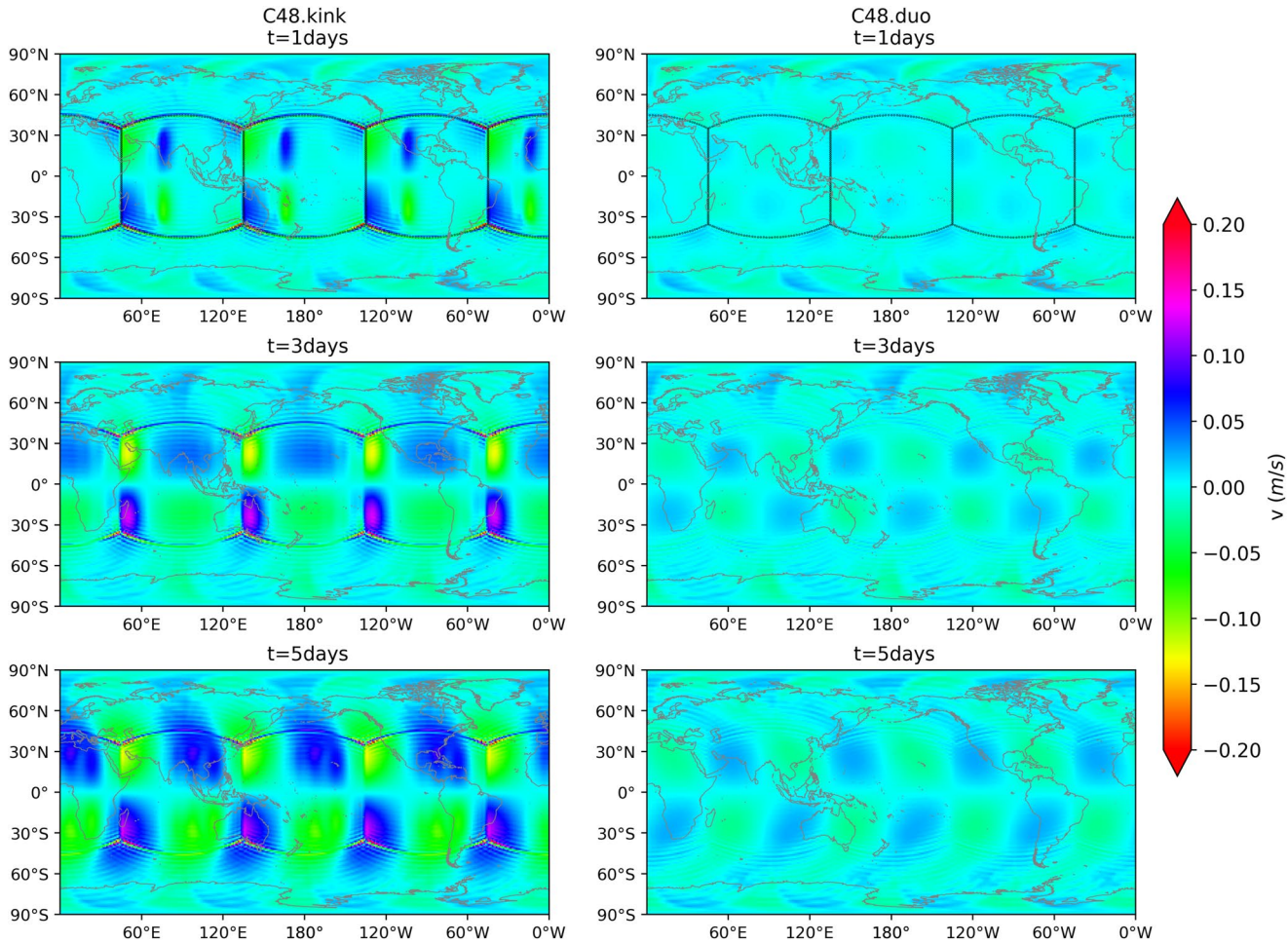

Figure 5. Spatial distribution of the meridional velocity errors of the C48 steady state geostrophic balance flow with a flow oriented perpendicular to the cubed-sphere edges at days = 1, 3 and 5. The advection scheme is 'MONO'. Grids edges are only plotted at day 1.

confirms that the Duo-Grid algorithm can remove both grid imprinting noise and some 2-delta instabilities while maintaining the dispersion and dissipation properties of the solver.

The wavenumber-4 Rossby-Haurwitz case is a strenuous dynamical core test. This is usually used to test the robustness of a dynamical core and assess its ability to preserve accuracy and symmetry in a simulation (Lin & Rood, 1997). Numerical errors arise in a run due to many reasons such as truncation and rounding errors of the advection scheme, edge handling, data interpolation, model formulation (i.e., choice of variable staggering) etc. These errors will build up in time and cause the propagating wave to lose its symmetry and eventually break. Typically a dynamical core should be able to maintain the basic wavenumber-4 structure for a minimum of 14 days (Lin & Rood, 1997). Figure 11 shows C48 simulations of this Rossby-Haurwitz test. The long timestep used here is 1200s with an acoustic timestep of 170s. We find that the kinked grid can maintain the symmetry of the wave for approximately 80 days; in contrast, the Duo-Grid will preserve the shape of the Rossby-wave beyond 100 days.

The colliding modons test case is used to evaluate vorticity dynamics in a dynamical core and as well as its ability to handle nonlinear rotational flows (Lin et al., 2017). Two modons are initialized at the equator; one traveling to the East and the other to the West. When they collide, they do not merge but they instead exchange positive/negative vortices and form two new modons with no change in their structure that propagate across opposite poles. They collide again at the equator, exchange vortices and again form two new modons that travel along the equator and return to their original positions. This would repeat indefinitely if the modons are not subjected to numerical diffusion and if there are no other numerical errors in the solver or grids which could cause the modon to break by disrupting the symmetry of the vortices. The ultimate aim of conducting this test is to assess the ability of the dynamical core to preserve flow symmetry and modon shape throughout the entire run for the

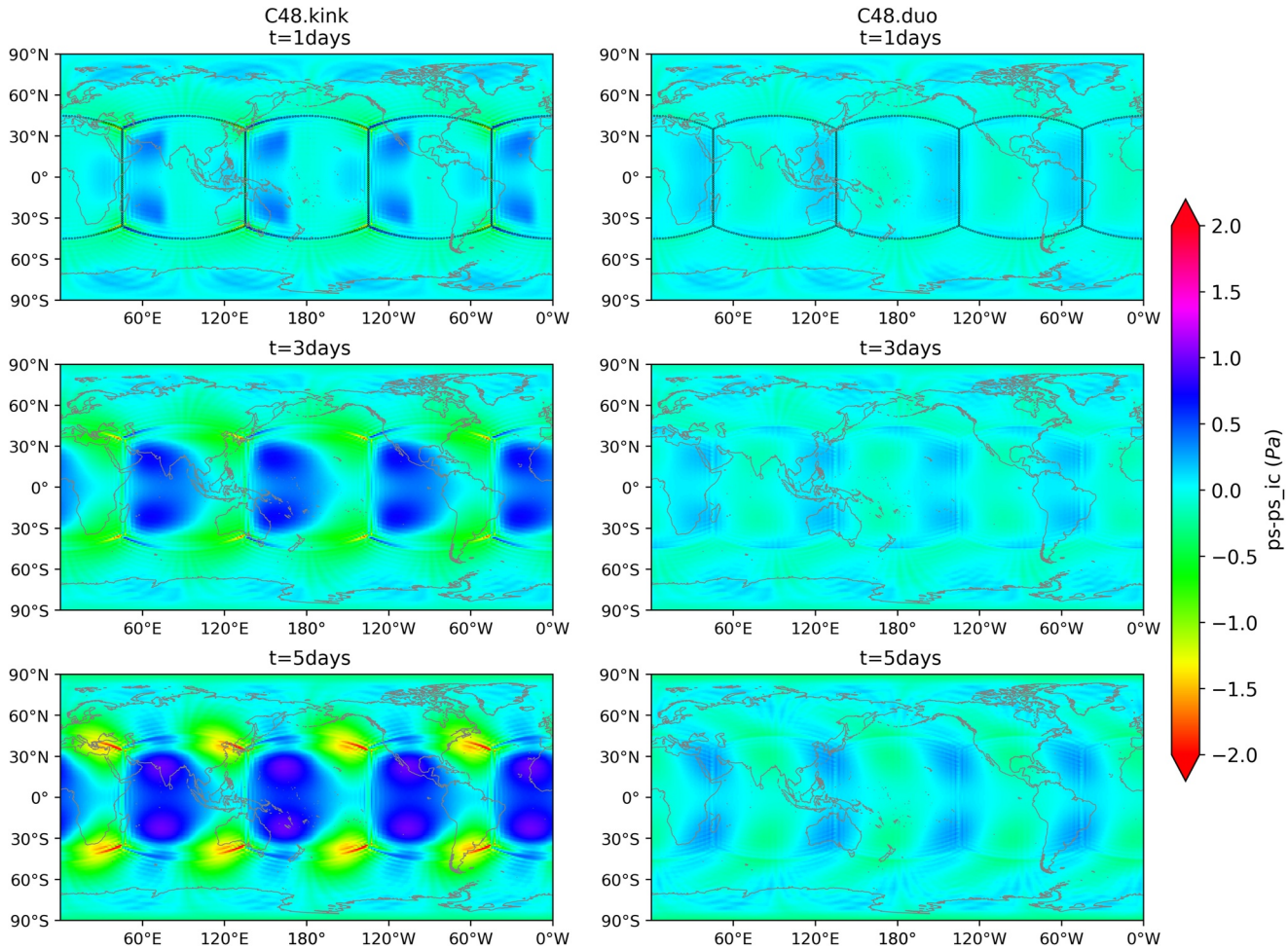

Figure 6. As in Figure 5 but for surface pressure errors.

longest possible time. Figure 12 shows the colliding modons simulation for a C48 grid for the advection scheme 'MONO' with and without the Duo-Grid system for two grid setups: On the left, modons cross the cubed-sphere edges perpendicularly ($\alpha = 0$), and on the right, modons cross cubed-sphere corners and edges obliquely ($\alpha = 45$). As can be seen, the modons are able to maintain their shape and come back to their initial positions. The modons' distortion at the north and south poles are simply due to the map projection on the 2D plane.

It is also worth noting that the modons are slightly faster and more diffused in the Duo-Grid case over a corner compared to the kinked grid case if one looks at their position at day 80. This is probably due to the modons traveling over coarser grids on the extended grid in the corner region compared to that in the kinked grid as shown in Figure 1: The grid cells in the gray region are slightly coarser than those of the blue and red regions. This comes at the expense of a smaller red region area due to the convergence of extended grid lines in the red halo area. Consequently, this leads to a more diffusive, slightly elliptic vortex structure that ends up propagating faster toward the end. Another possible cause could be the 1D linear interpolation scheme. A more in-depth analysis can be done here to analyze the final shape and amplitude of the modons and the effects of higher order 1D or 2D interpolation schemes and will be reported in future work.

3.2. Three-Dimensional Solvers

We test here the dry baroclinic wave as described in Jablonowski and Williamson (2006) using the 3D non-hydrostatic solver. These simulations are initialized with a three-dimensional baroclinically unstable zonally symmetric atmosphere with a perturbation in the northern hemisphere to trigger development of a baroclinic wave. Ideally there should be no deviation from zonal symmetry in the southern hemisphere; errors due to grid imprinting will grow in this unstable atmosphere. We consider 32 vertical layers in order to be consistent with

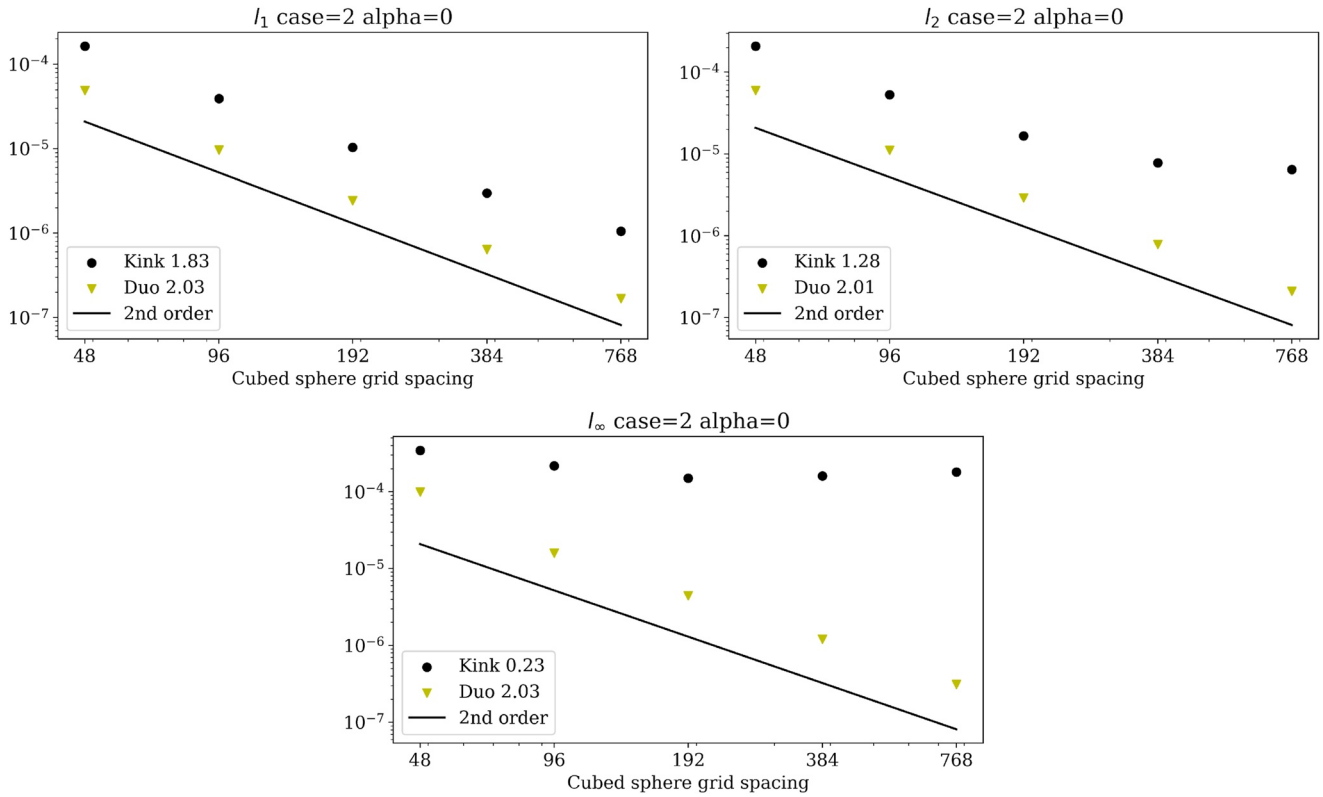

Figure 7. Convergence of absolute 5-day error norms l_1, l_2, l_∞ for the steady state geostrophic test case and a flow oriented perpendicular to the cubed-sphere edges ($\alpha = 0$) for different resolutions C48, C96, C192, C384 and C768. The advection scheme is 'MONO'. Convergence rates are given in the legends.

previous studies. The advection scheme used here is 'MINDIFF' with a vorticity damping coefficient of 0.12. We aslo use sixth-order divergence damping with a nondimensional coefficient of 0.12 similar to that of the shallow water test cases. Here, the long timestep is 1920 s, the number of vertical remappings per long timestep is 1 and the number of acoustic timesteps per vertical remapping timestep is eight yielding an acoustic time-step of 240 s. The time-step used for higher resolution runs C96, C192, C384 and C768 in what follows is chosen so that the Courant number is conserved in all cases. Rayleigh damping is turned off and no sponge layers are considered at the top of the computational domain. We also tested the hydrostatic solver and found no noticeable difference in the results.

Figure 13 illustrates snapshots of the meridional velocity field on days 6, 7, 8, and 9 for a C48 resolution with and without the Duo-Grid system. As can be seen, numerical errors are generated at the corners of the cubed-sphere in both the northern and southern hemispheres. These errors are present in the Duo-Grid case but have a much lower magnitude, as seen later in Figure 15. This will also be discussed in the error norm plots.

Figure 14 shows snapshots of the surface pressure field in the southern hemisphere at day 9 for different grid resolutions: C48 (200 km), C96 (100 km), C192 (50 km), C384 (25 km), C768(13 km) with and without Duo-Grid. The pressure field in the southern hemisphere should remain undisturbed, meaning that any deviation from the uniform surface pressure field is considered an error. We can see in Figure 14 a similar behavior to that of Figure 13, that is, in the cases without Duo-Grid, noise is still generated but decreases with increasing resolution. On the other hand, we can see that in the Duo-Grid cases (right column), these errors are practically non-existent.

Furthermore, to quantify these errors and check their magnitude, we compute error norms l_1, l_2 and l_∞ of the surface pressure field in the southern hemisphere. Figure 15 shows the time evolution of these errors for grid resolutions C48, C96, C192 C384, and C768. As previously mentioned, any deviation from the initial surface pressure field is considered erroneous. Therefore, the initial condition of the flow state is considered a true solution. The runs with the Duo-Grid clearly have lower errors compared to those without it. Furthermore, the error norms' magnitudes decrease with increasing resolution, indicating convergence of the solution. It is worth noting that these errors, for the time considered in these simulations, oscillate around a mean value and do not dramatically increase as they do in the kinked-grid simulations. Note especially that the l_∞ errors, which grow exponentially on

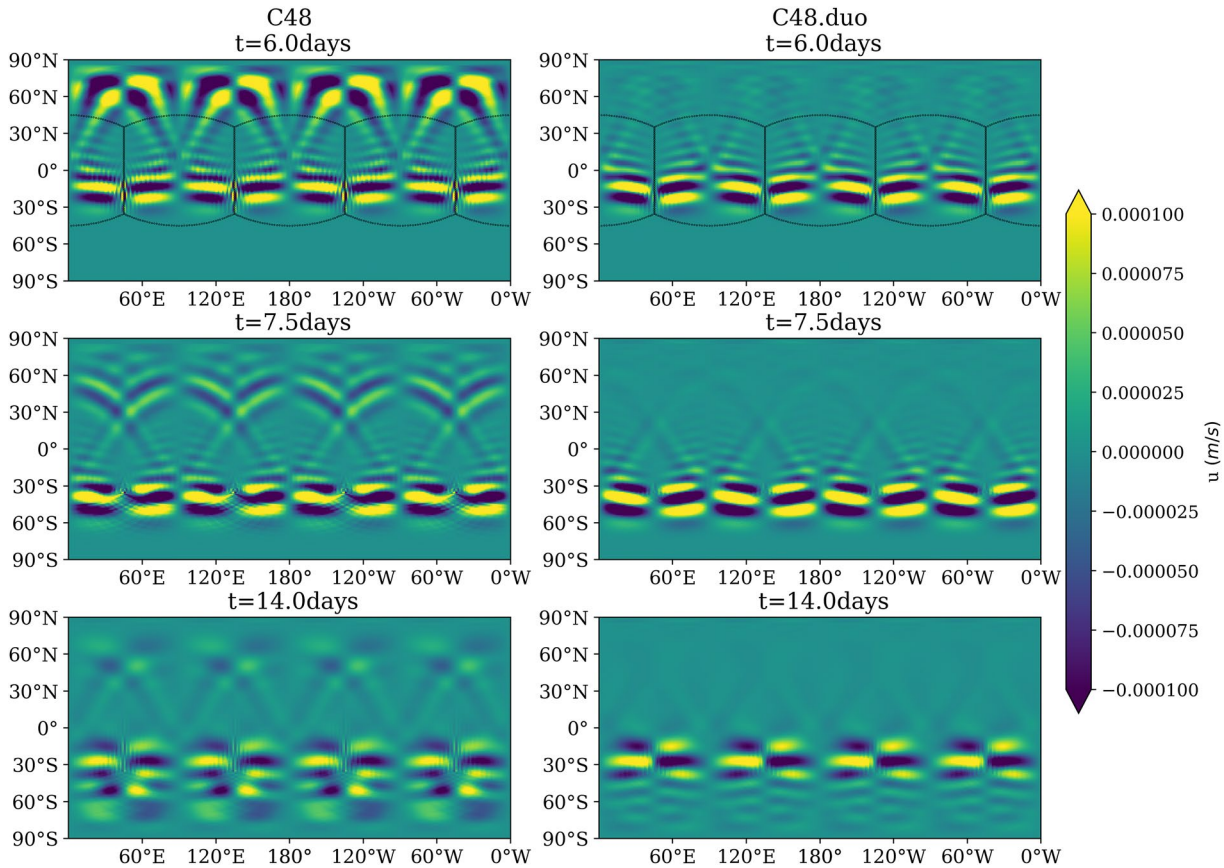

Figure 8. Spatial distribution of the zonal velocity errors of the C48 splash test case at days = 6, 7.5 and 14 days. The advection scheme is 'MONO'. Grids edges are only plotted at day 6.

the kinked-grid, remain bounded on the Duo-Grid, indicating that the deviations from the initial uniform surface pressure are primarily modes that are not the unstable baroclinic mode.

Additionally, we ran the baroclinic wave test case for a longer time of 14 days, giving more time for the exponentially growing baroclinic instabilities to develop. We noticed that some grid imprinting became apparent with the Duo-Grid, but compared to the kinked grid was an order of magnitude smaller at C48 and two orders of magnitude smaller at C384. We suspect that this might be caused by the flux averaging procedure at the face edges introducing a weak discontinuity, or that the error could be reduced further by introducing a higher-order 1D interpolation method or a 2D interpolation to more accurately remap the data in the halo. At this point we believe that the grid imprinting error is sufficiently small that more complex or expensive interpolations are unnecessary.

As has been noted in the geostrophic and baroclinic tests, numerical noise is produced at the edges of the kinked grid. The large localized errors at the edges are captured by l_∞ which increases with simulation time (sometimes exponentially as seen the baroclinic case). These errors will propagate into the interior of the cube faces and contaminate the numerical solution driving up l_1 and l_2 errors within a few days. The Duo-Grid reduces the errors produced at the edges of the cubed-sphere grid, keeping l_∞ low and thus also l_1 and l_2. This, along with the results of the Rossby-Haurwitz wave test case and the convergence rates of the geostrophic flow test case clearly indicate an improvement in numerical robustness of FV3 when using the Duo-Grid.

4. Ongoing Work

The current implementation of the Duo-Grid is computationally more expensive than when using the kinked grid. This slowdown is caused by the remapping from kinked to extended grids, as well as the various edge flux averaging processes that necessitate additional MPI communication calls among processors located on edges. Ongoing work is in progress to optimize the current implementation. One intrinsic computational advantage of

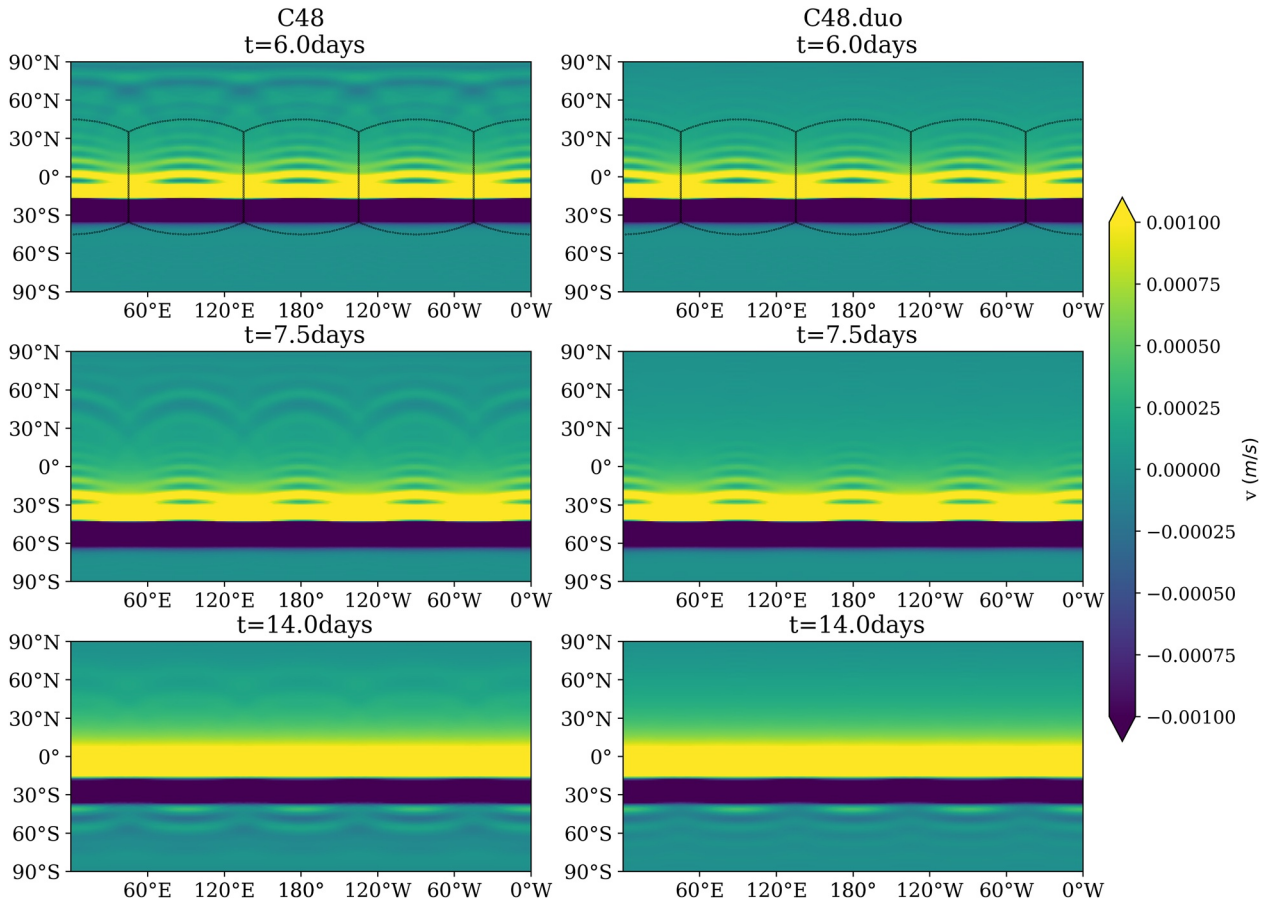

Figure 9. Meridional velocity field of the C48 splash test case at days = 6, 7.5, and 14 days. The advection scheme is 'MONO'. Grids edges are only plotted at day 6. Note that the scale is shrunk to show lower order noise.

the Duo-Grid is that it eliminates the need for edge handling within the solver algorithms, especially the advection scheme, and thereby can maintain steady computational work throughout the domain during the integration. This can yield significant performance gains on Graphical Programming Unit (GPU) processors, since the edge handling is currently a significant bottleneck on these systems (Dahm et al., 2022). Future work will also describe full-physics simulations with the Duo-Grid.

5. Conclusions

We have implemented the Duo-Grid in FV3. The Duo-Grid halo remapping consists of remapping the halo data from its neighboring faces from their 'kinked' locations to their corresponding natural locations on the extended

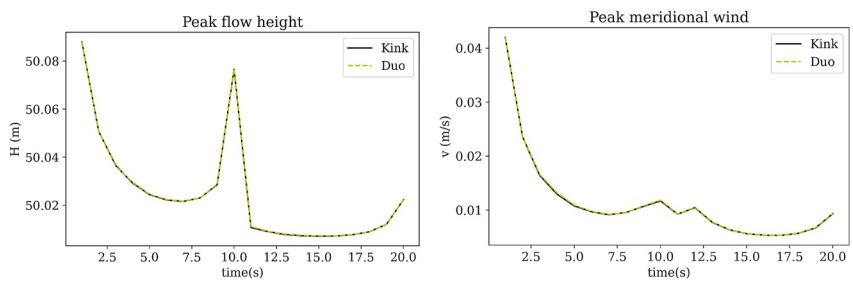

Figure 10. Time evolution of peak flow height and peak meridional winds of the C48 splash test case. The advection scheme is 'MONO'.

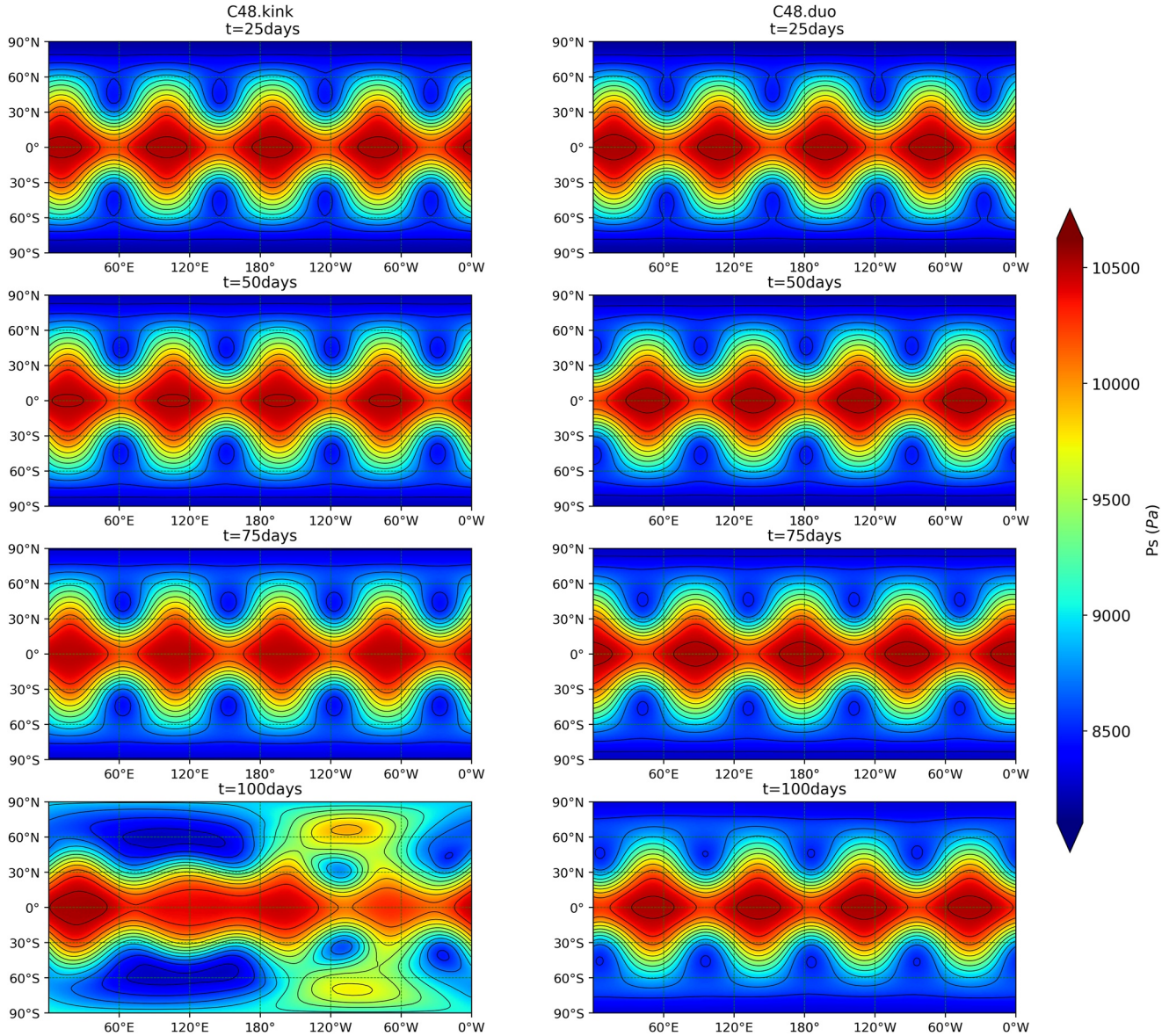

Figure 11. Surface pressure contour lines of a C48 Rossby-Haurwitz test wave with a flow oriented perpendicular to the cubed-sphere edges at days = 25, 50, 75, and 100 days. The contour interval is 200 Pa. The dashed lines are the gridded latitudes and longitudes with intervals of 30 and 45°, respectively. The advection scheme is 'MONO'.

grid. Edge flux synchronization is performed to ensure conservation properties following the remapping onto the extended grid.

We test various cases using the Duo-Grid in the shallow water solver. In particular, we focus on the cases of the steady state geostrophic balanced flow, the splash on the sphere, the Rossby-Haurwitz wave and the colliding modons. Different flow configurations, advection schemes, grid resolutions were examined. Errors norms l_1, l_2 and l_∞ were computed to quantify errors in the numerical solution. It is shown that the current implementation of the Duo-Grid decreases the growth rate of these errors in all cases. In particular, l_∞ is reduced by up to an order of magnitude comparing to kinked-grid simulations. Moreover, results show that the Duo-Grid conserves the order of accuracy of FV3's horizontal discretization and results from the splash on the sphere test demonstrate that the Duo-Grid algorithm displays dispersion and dissipation properties that are identical to those of the original FV3 algorithm. In addition, the results of the Rossby wave tests indicate that the dynamical core has been made more robust by the Duo-Grid.

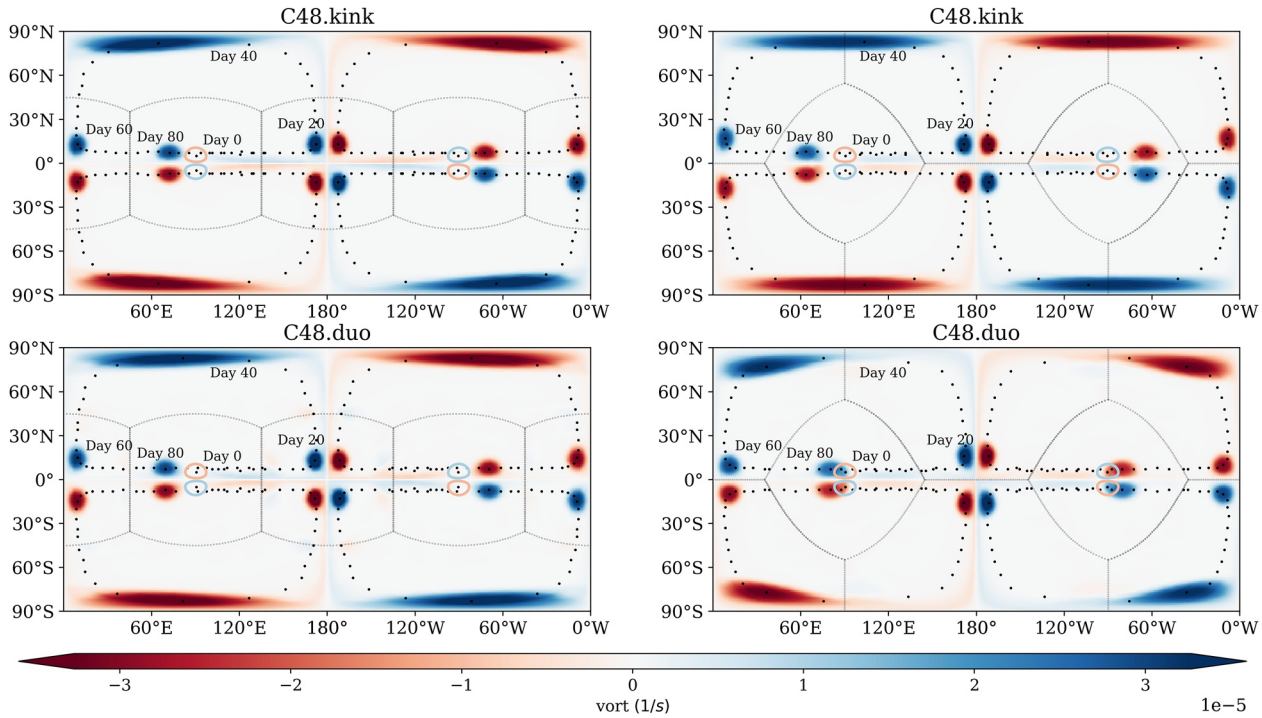

Figure 12. Time evolution of the colliding modon case for a C48 case. The points represent the center positions of the two vortices of each modon every 2 days during the 100 days simulations. Left panels: modons cross cubed-sphere edges. Right panels: modons cross corners. Top panels show the kinked grid and bottom panels show the Duo-Grid. Open contours represent the modons' initial locations. The advection scheme is 'MONO'.

We also test the Duo-Grid in a three-dimensional baroclinic wave test case. We observe the same behavior as in the shallow water tests: runs with the Duo-Grid produce lower numerical errors, which decrease further with resolution. Grid imprinting was almost non-existent with the Duo-Grid at the ninth day; in particular deviations from zonal symmetry in the southern hemisphere were comparable to other numerical errors and gravity waves in the solution. Moreover, for higher resolution runs, we observed a stabilizing effect for the Duo-Grid where errors oscillate around a mean value and do not amplify and contaminate the entire numerical solution in question. Further work will optimize the computational performance of the Duo-Grid algorithm and to test the method in full physics simulations as well as investigating other interpolation methods in the halo area and exploring different techniques to conserve properties at the edges other than the current flux averaging.

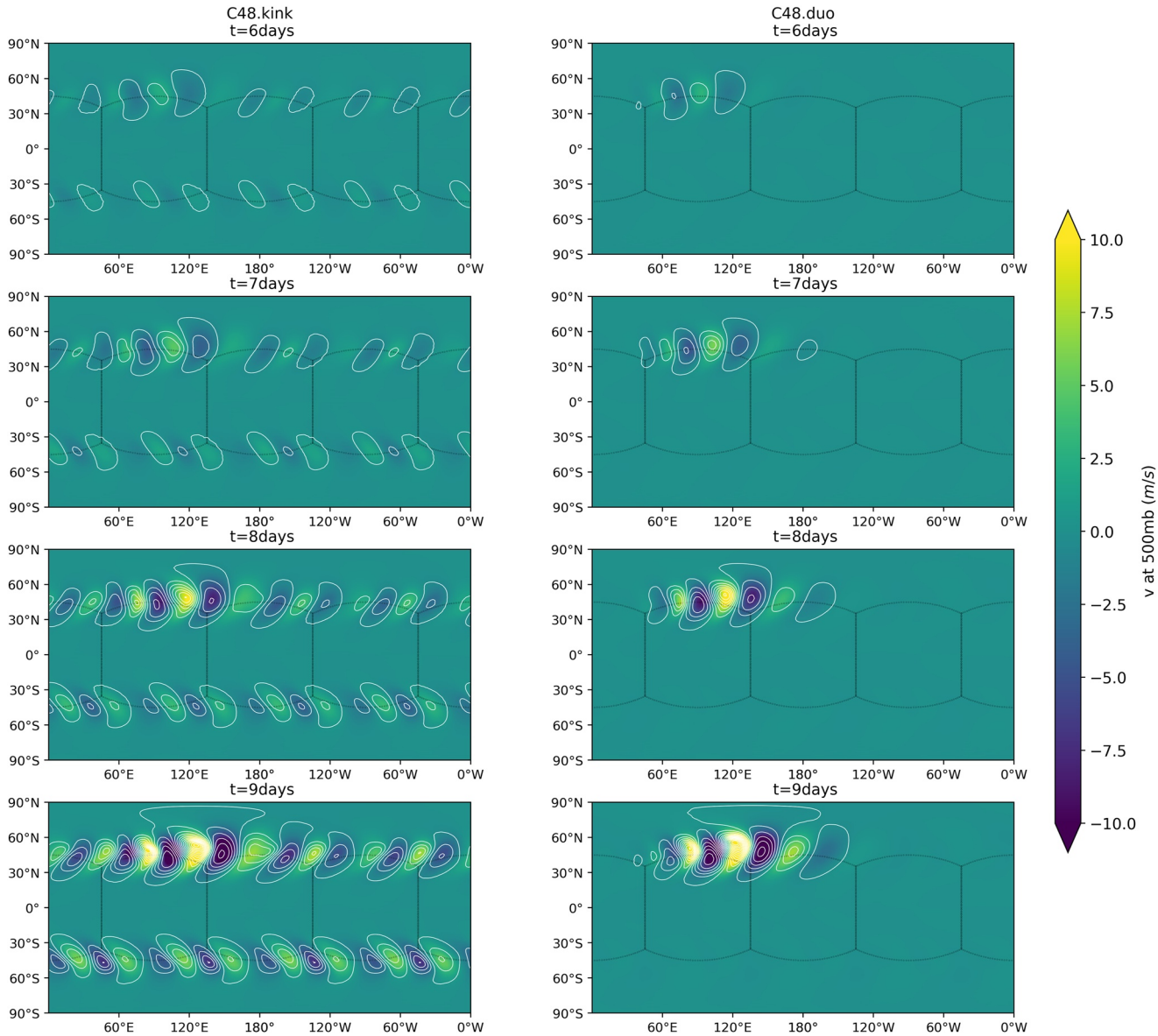

Figure 13. Snapshots of meridional winds at 500mb for the C48 3D baroclinic wave test case on a C48 grid at days 6, 7, 8 and 9. Contour lines represent pressure with an interval of 20 Pa around the mean 1,000 mb pressure field. The advection scheme is 'MINDIFF'.

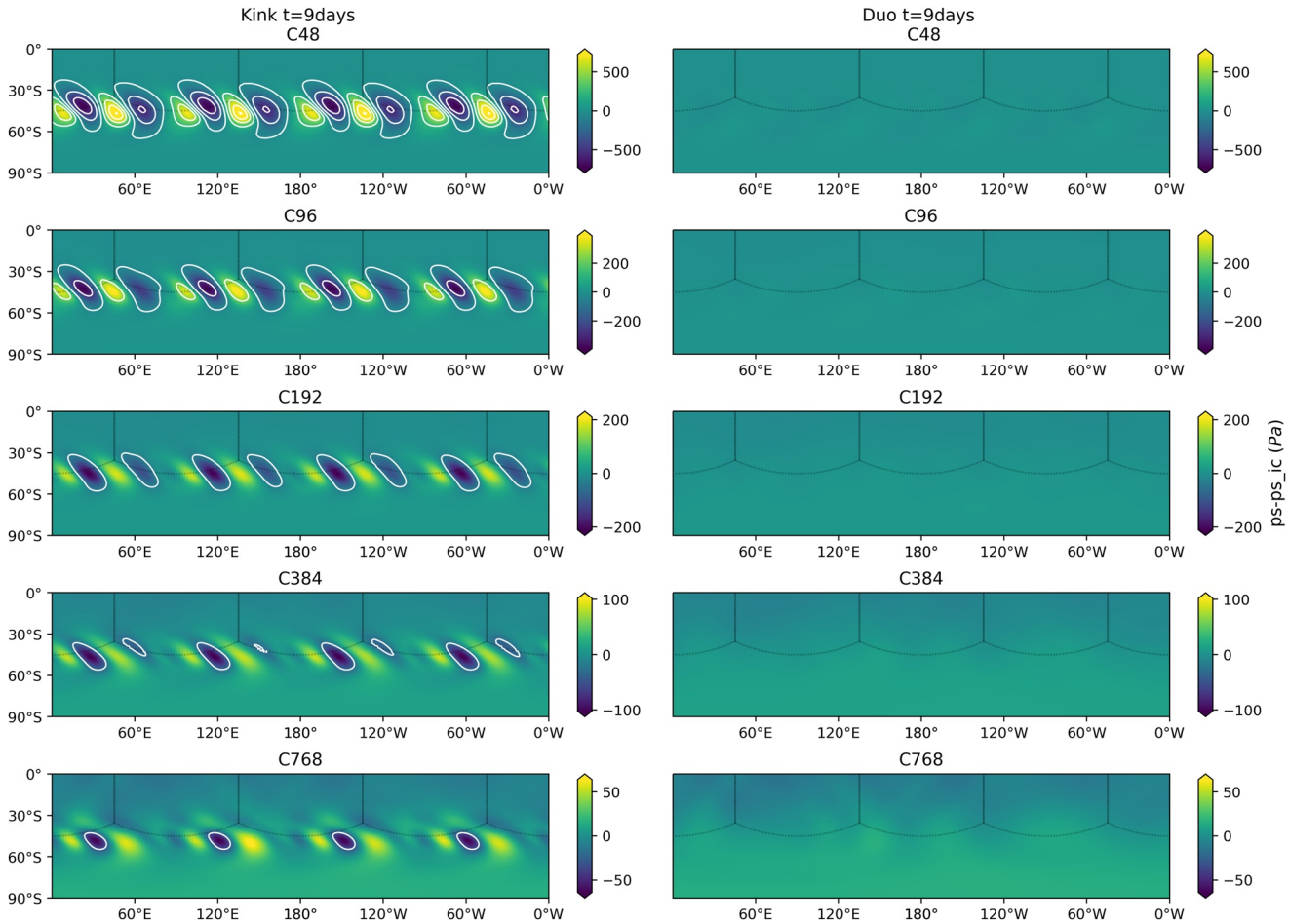

Figure 14. Error map of the surface pressure in the southern hemisphere for the baroclinic wave test case for different resolutions C48, C96, C192, C384 and C768 at day 9. Contour lines represent pressure lines with an interval of 20 Pa. The advection scheme is 'MINDIFF'.

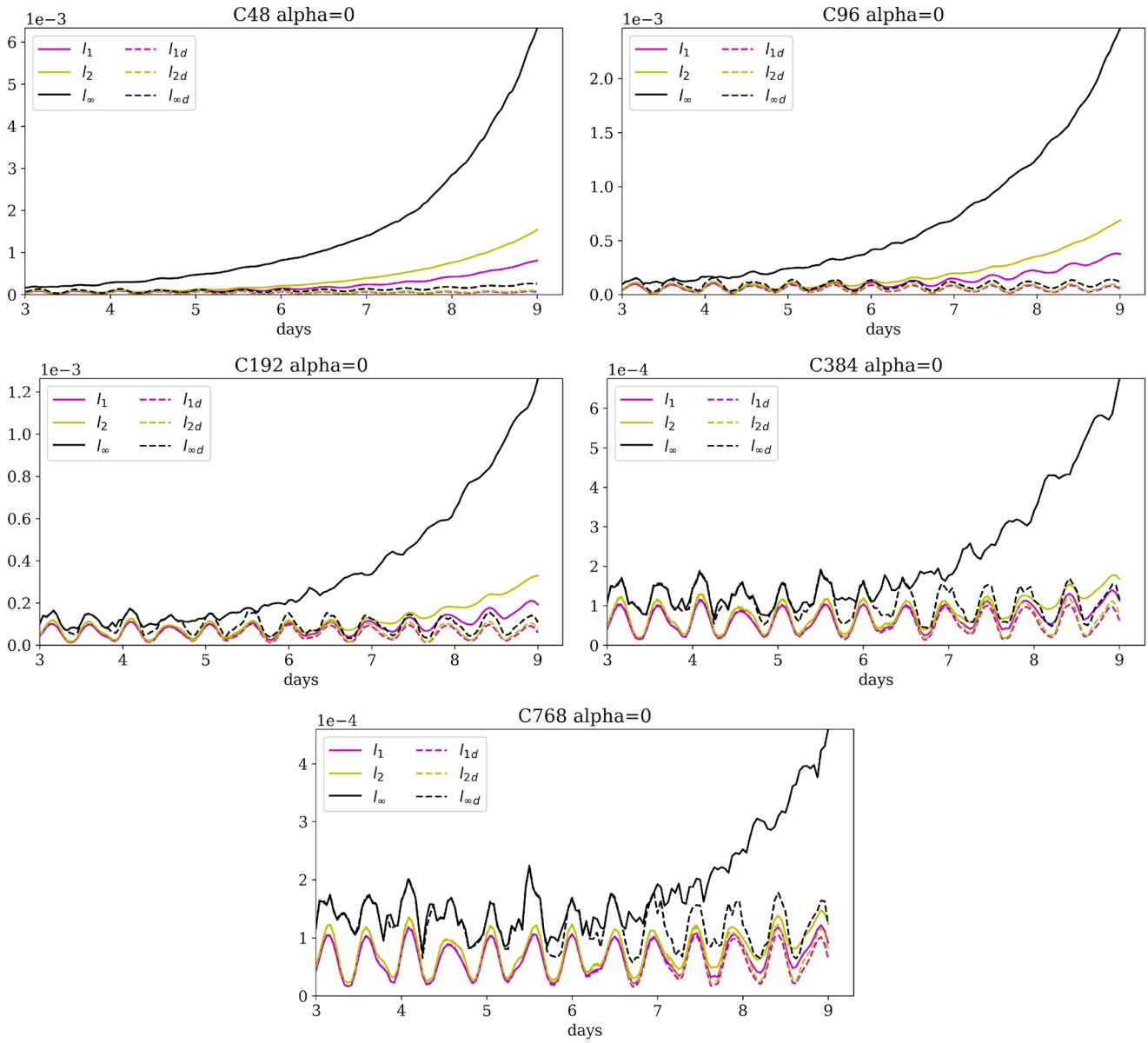

Figure 15. Time evolution of error norms l_1, l_2 and l_∞ in the southern hemisphere for the baroclinic wave test case for different resolutions C48, C96, C192 C384 and C768. Error norms obtained on the kinked grid are represented by solid lines while those on the Duo-Grid are represented by dashed lines.

Disclaimer

The statements, findings, conclusions, and recommendations are those of the author(s) and do not necessarily reflect the views of the National Oceanic and Atmospheric Administration, or the US Department of Commerce.

Conflict of Interest

The authors declare no conflicts of interest relevant to this study.

Data Availability Statement

GFDL's Finite-Volume Cubed-Sphere Dynamical Core (FV3) official releases are all available on GFDL's GitHub site (https://github.com/NOAA-GFDL, last access: 17 December 2023). The code used in this paper is still under development. The corresponding source code and data are publicly available (Mouallem, 2023).

Acknowledgments
The authors express their gratitude to Rusty Benson for many insightful discussions and valuable assistance during this project. We would like to thank Oliver Elbert and Rusty Benson for their reviews and useful comments that improved the quality of the manuscript. Finally, the authors extend their appreciation to the two anonymous referees for their careful assessment and valuable comments. Joseph Mouallem is funded by the National Oceanic and Atmospheric Administration, US Department of Commerce (Grant NA18OAR4320123, NA19OAR0220143 and NA19OAR0220147), NOAA's Weather Program Office, and the NOAA Research Global-Nest Initiative. Xi Chen is funded by the National Natural Science Foundation of China (Grant 42275174 and 42288101).

References

Arakawa, A., & Lamb, V. R. (1977). Computational design of the basic dynamical processes of the UCLA general circulation model. *Methods in Computational Physics: Advances in Research and Applications*, *17*, 173–265. https://doi.org/10.1016/B978-0-12-460817-7.50009-4

Chen, X. (2021). The LMARS based shallow-water dynamical core on generic gnomonic cubed-sphere geometry. *Journal of Advances in Modeling Earth Systems*, *13*, 1–31. https://doi.org/10.1029/2020MS002280

Chen, X., Andronova, N., Leer, B. V., Penner, J. E., Boyd, J. P., Jablonowski, C., & Lin, S. J. (2013). A control-volume model of the compressible Euler equations with a vertical Lagrangian coordinate. *Monthly Weather Review*, *141*(7), 2526–2544. https://doi.org/10.1175/MWR-D-12-00129.1

Dahm, J., Davis, E., Deconinck, F., Elbert, O., George, R., McGibbon, J., et al. (2022). Pace v0.1: A python-based performance-portable implementation of the FV3 dynamical core. *EGUsphere*, *2022*, 1–24. https://doi.org/10.5194/egusphere-2022-943

Diamantakis, M., & Agusti-Panareda, A. (2017). *A positive definite tracer mass fixer for high resolution weather and atmospheric composition forecasts (No. 819)*. ECMWF. https://doi.org/10.21957/qpogzoy

Harris, L., Chen, X., Putman, W., Zhou, L., & Chen, J.-H. (2021). A scientific description of the GFDL Dynamical Core, *C*, 1–109. https://doi.org/10.25923/6nhs-5897

Harris, L. M., & Lin, S. J. (2013). A two-way nested global-regional dynamical core on the cubed-sphere grid. *Monthly Weather Review*, *141*(1), 283–306. https://doi.org/10.1175/MWR-D-11-00201.1

Harris, L. M., Lin, S.-J., & Tu, C. (2016). High-resolution climate simulations using GFDL HiRAM with a stretched global grid. https://doi.org/10.1175/JCLI-D-15-0389.s1

Jablonowski, C., & Williamson, D. L. (2006). A baroclinic instability test case for atmospheric model dynamical cores. *Quarterly Journal of the Royal Meteorological Society*, *132*(621C), 2943–2975. https://doi.org/10.1256/qj.06.12

Katta, K. K., Nair, R. D., & Kumar, V. (2015). High-order finite-volume transport on the cubed sphere: Comparison between 1d and 2d reconstruction schemes. *Monthly Weather Review*, *143*(7), 2937–2954. https://doi.org/10.1175/MWR-D-13-00176.1

Lin, S. J. (2004). A "vertically Lagrangian" finite-volume dynamical core for global models. *Monthly Weather Review*, *132*(10), 2293–2307. https://doi.org/10.1175/1520-0493(2004)132⟨2293:AVLFDC⟩2.0.CO;2

Lin, S. J., Harris, L., Chen, X., Yao, W., & Chai, J. (2017). Colliding modons: A nonlinear test for the evaluation of global dynamical cores. *Journal of Advances in Modeling Earth Systems*, *9*(7), 2483–2492. https://doi.org/10.1002/2017MS000965

Lin, S.-J., & Rood, R. B. (1996). Multidimensional flux-form semi-Lagrangian transport schemes. *Monthly Weather Review*, *124*(9), 2046–2070. https://doi.org/10.1175/1520-0493(1996)124⟨2046:MFFSLT⟩2.0.CO;2

Lin, S.-J., & Rood, R. B. (1997). An explicit flux-form semi-Lagrangian shallow-water model on the sphere. *Quarterly Journal of the Royal Meteorological Society*, *123*(544), 2477–2498. https://doi.org/10.1002/qj.49712354416

Mouallem, J. (2023). Implementation of the novel duo-grid in GFDL's FV3 dynamical core - code and simulations files [Software] [Dataset]. Zenodo. https://doi.org/10.5281/zenodo.8327578

Mouallem, J., Harris, L., & Benson, R. (2022). Multiple same-level and telescoping nesting in GFDL's dynamical core. *Geoscientific Model Development*, *15*(11), 4355–4371. https://doi.org/10.5194/gmd-15-4355-2022

Peixoto, P. S., & Barros, S. R. (2013). Analysis of grid imprinting on geodesic spherical icosahedral grids. *Journal of Computational Physics*, *237*, 61–78. https://doi.org/10.1016/j.jcp.2012.11.041

Putman, W. M., & Lin, S. J. (2007). Finite-volume transport on various cubed-sphere grids. *Journal of Computational Physics*, *227*(1), 55–78. https://doi.org/10.1016/j.jcp.2007.07.022

Rančić, M., Purser, R. J., Jović, D., Vasic, R., & Black, T. (2017). A nonhydrostatic multiscale model on the uniform Jacobian cubed sphere. *Monthly Weather Review*, *145*(3), 1083–1105. https://doi.org/10.1175/MWR-D-16-0178.1

Ullrich, P. A., Jablonowski, C., & van Leer, B. (2010). High-order finite-volume methods for the shallow-water equations on the sphere. *Journal of Computational Physics*, *229*(17), 6104–6134. https://doi.org/10.1016/j.jcp.2010.04.044

Weller, H., Thuburn, J., & Cotter, C. (2012). Computational modes and grid imprinting on five quasi-uniform spherical c grids. *Monthly Weather Review*, *140*(8), 2734–2755. https://doi.org/10.1175/mwr-d-11-00193.1

Whitaker, J. (2015). *HIWPP non-hydrostatic dynamical core tests: Results from idealized test cases* (p. 28). NOAA/ESRL/PSD. Retrieved from https://www.weather.gov/media/sti/nggps/HIWPP_idealized_tests-v8%20revised%2005212015.pdf

Williamson, D. L., Drake, J. B., Hack, J. J., Jakob, R., & Swarztrauber, P. N. (1992). A standard test set for numerical approximations to the shallow water equations in spherical geometry. *Journal of Computational Physics*, *102*(1), 211–224. https://doi.org/10.1016/S0021-9991(05)80018-6

Zerroukat, M., & Allen, T. (2022). On the corners of the cubed-sphere grid. *Quarterly Journal of the Royal Meteorological Society*, *148*(743), 778–783. https://doi.org/10.1002/qj.4230

Zhao, M., Golaz, J.-C., Held, I. M., Guo, H., Balaji, V., Benson, R., et al. (2018). The GFDL global atmosphere and land model AM4.0/LM4.0: 2. Model description, sensitivity studies, and tuning strategies. *Journal of Advances in Modeling Earth Systems*, *10*(3), 735–769. https://doi.org/10.1002/2017MS001209